Structural, Optical, and Magnetic Properties of Erbium-Substituted Yttrium Iron Garnets

Yujin Cho, Seohui Kang, Yeon Woo Nahm, Ahmed Yousef Mohamed, Yejin Kim, Deok-Yong Cho,* and Suyeon Cho*

Read Online

ACCESS | Metrics & More | Article Recommendations

ABSTRACT: We synthesized a series of slightly erbium-substituted yttrium iron garnets (Er:YIG), $Y_{3-x}Er_xFe_5O_{12}$ at different Er concentrations ($x = 0$, 0.01, 0.05, 0.10, and 0.20) using a solid-state reaction and investigated their structural, magnetic, and optical properties as a function of Er concentration. The volume of the unit cell slightly increased with Er concentration and Er atoms predominately replaced Y atoms in the dodecahedrons of YIG. The optical properties exhibited certain decreases in reflectance in the 1500−1600 nm wavelength range due to the presence of Er^{3+}. Despite the many unpaired 4f electrons in Er^{3+}, the total magnetic moments of Er:YIG showed similar trends with temperatures and magnetic fields above 30 K. An X-ray magnetic circular dichroism study confirmed the robust Fe 3d magnetic moments. However, the magnetic moments suddenly decreased to below 30 K with Er substitution, and the residual magnetism (M_R) and coercive field

(H_C) in the magnetic hysteresis loops decreased to below 30 K with Er substitution. This implies that Er substitution in YIG has a negligible effect on magnetic properties over a wide temperature range except below 30 K where the Er 4f spins are coupled antiparallel to the majority Fe 3d spins. Our studies demonstrated that above 30 K the magnetic properties of YIG are retained even with Er substitution, which is evidence that the Er doping scheme is applicable for YIG-based magneto-optical devices in the mid-infrared regime.
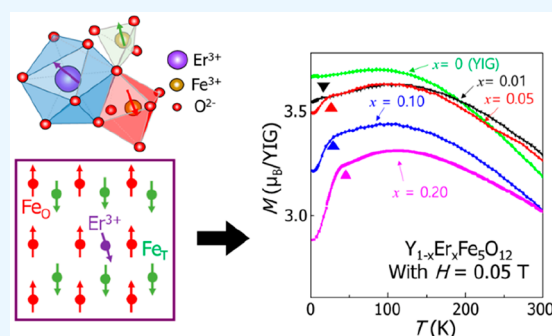
I. INTRODUCTION

Magnetic garnets have been regarded as key materials for quantum computing and communication systems because of their intriguing quantum phenomena, such as hybridized magnon−phonon excitation,[1] the conversion between magnons and phonons,[2] spin pumping with elastic waves,[3] and the spin Seebeck effect,[4] which are based on a strong magnon and phonon interactions. Compared with the magnon−phonon interaction in dilute spin ensemble systems such as rare-earth ion-doped crystals[5] or nitrogen-vacancy centers in diamonds,[6] insulating ferrimagnet yttrium iron garnets ($Y_3Fe_5O_{12}$, YIG) have been widely used for various magneto-optical applications. Many researchers have made efforts to achieve a high spin density and a low damping rate, which are important factors for magnetic spintronic devices, as well as high-frequency microwave devices.[7−10]

It has been reported that transition-metal-substituted YIG exhibits a giant Faraday rotation or a magneto-optical Kerr effect, indicating that the interaction between magnetic and optical properties can be modulated by substitution or doping in the YIG system.[11−13] Rare-earth atoms substituted garnets have attracted much attention for optical applications because of their strong fluorescence emission in the mid-infrared

regime.[14] Er-substituted crystals exhibit a high radiative decay rate and a long optical coherent time, as well as mid-infrared emissions at a wavelength of 1.5 μm, which is the C-band for telecommunications.[15] In recent years, the magnetic, optical, and structural properties of rare earth or transition-metal-substituted garnets have been widely investigated. Ce-substituted YIG has enhanced magnetic moments because of the preferred-(100) orientation.[16] The coercive fields of magnetic garnets have been studied by changing the grain sizes.[17,18] However, many garnets with substitutional atoms have shown degraded magnetic and optical properties due to changes of sample properties such as crystallinity, shape, size, and impurities.[19,20] Therefore, the search for appropriate substitutional atoms to enhance the magnetic properties as well as optical properties is highly demanded.
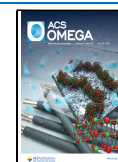
Here, we synthesized a series of Er-substituted YIG, which had the chemical compositions of $Y_{3-x}Er_xFe_5O_{12}$ at different Er concentrations (x = 0, 0.01, 0.05, 0.10, and 0.20) using a solid-state reaction method, and studied their changed magnetic and optical properties with small concentrations of Er atoms. Fe $L_{2,3}$-XAS and XMCD spectra showed that the Er atoms seemed to replace Y atoms in the dodecahedrons of YIG. We found that the optical properties were almost invariant under Er substitution except for small changes in reflectance in the range of 1500−1600 nm wavelengths because of the distinct optical transition lines of the Er^{3+} ions. The magnetic properties of YIG were retained in a moderate temperature range, 30−300 K, however, below 30 K the magnetic moment and coercive force decreased as functions of the Er concentration, indicating an antiparallel spin alignment of the Er 4f spins at Y sites below that temperature. Our study showed that the magnetic properties of YIG could be retained in a broad temperature range of 30−300 K with characteristic optical transition lines in a range relevant to optical telecommunication systems when Er atoms were substituted in YIG at small concentrations.

II. EXPERIMENTAL PROCEDURES

II.1. Sample Synthesis. Powders of $Y_{3-x}Er_xFe_5O_{12}$ were synthesized by a solid-state reaction with various Er contents (x). The stoichiometric mixtures of high purity powders, Y_2O_3 (99.99%, Sigma-Aldrich), Fe_2O_3 (99.995%, Sigma-Aldrich), and Er_2O_3 (99.9%, Sigma-Aldrich), were well ground using an agate mortar. These mixtures were calcined at 850 °C for 12 h, then cooled down to room temperature in air. This mixture was reheated three times to a high temperature of 1300 °C with intermediate grinding.

II.2. Sample Characteristics. We studied the crystal structures of the Er-substituted YIG using X-ray powder diffraction (Expert pro-MPD, PANalytical) at the Western Seoul Center of Korea Basic Science Institute (KBSI) using Cu Kα radiation (λ = 0.15406 nm) in the 2θ range of 10−120° at room temperature. The actual Er concentration in Er-substituted YIG was also studied using an inductively coupled plasma optical emission spectrometer (ICP-OES) (OPTIMA 5110, Agilent) at the Yonsei Center for Research Facilities (YCRF). Differential scanning calorimetry (DSC250, TA Instruments) at Ewha Womans University was used to estimate the Curie temperatures of the Er-substituted YIG in a temperature range of 300−700 K. A SQUID Magnetometer (Quantum Design MPMS3, Quantum Design North America) at the KBSI was used to observe the magnetic properties of Er-substituted YIG in a temperature range of 2−300 K from −0.1 to 0.1 T. The optical properties of the Er-substituted YIG were determined by Fourier-transform infrared spectroscopy (Nicolet iS50, Thermo Fisher Scientific Instrument) and a UV−VIS/NIR spectrophotometer (Lambda 1050, Perkin Elmer) at the KAIST Analysis Center for Research Advancement (KARA) within a wavelength range of 400−7000 cm^{-1}.

X-ray absorption spectroscopy (XAS) at the Fe $L_{2,3}$-edge of the powder samples was conducted at 2A beamline in the Pohang Light Source (PLS) at room temperature using circularly polarized X-rays. The absorption coefficient was collected as the total electron yield as a function of increasing photon energy. An external magnetic field of 0.7 T was applied during the measurement parallel and antiparallel to the normal direction of the specimen, and the difference in the absorption intensities (so-called X-ray magnetic circular dichroism; XMCD) was monitored to examine the long-range magnetic

moments of Fe 3d spins. Hard XAS at the Er L_3-edge was conducted at the 8C beamline at the PLS. The extended X-ray absorption fine structure (EXAFS) analysis was processed using the UWXAFS package.[21]

III. RESULTS AND DISCUSSION

Figure 1 shows a schematic of Er-substituted $Y_3Fe_5O_{12}$ (Er:YIG) with a cubic structure (space group Ia-3d). One
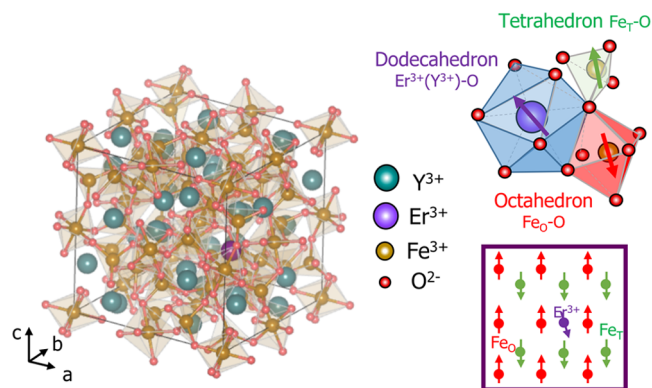

Figure 1. Crystal structure of YIG. One unit cell of YIG contains 24 dodecahedrons of Y−O, 24 octahedrons of Fe_O−O, and 16 tetrahedrons of Fe_T−O connected to each other by shared edges and corners.

unit cell contains $Y_{24}Fe_{40}O_{96}$ as shown in the inset of Figure 1. Since Y atoms with a trivalent state (Y^{3+}) have no magnetic moment, the net magnetic moment of YIG is determined by two different Fe^{3+} atoms, which align antiferromagnetically along the (110) crystal direction of the YIG. For convenience, the Fe atoms in the octahedral and tetrahedral coordination are designated as Fe_O and Fe_T, respectively. Fe_O and Fe_T have opposite spin directions, resulting in an expected magnetic moment of 5 μ_B/YIG at 0 K, which is consistent with the experimental value of 4.73 μ_B/YIG.[22] Since Er atoms have large magnetic moments and strong emission at around 1550 nm, the magnetic and optical properties of YIG might be modified by Er substitution. We synthesized polycrystalline Er-substituted YIG powders with chemical compositions of $Y_{3-x}Er_xFe_5O_{12}$ (x = 0, 0.05, 0.10, 0.15, and 0.20) and characterized their magnetic and optical properties as functions of the Er concentration. To prevent the unexpected formation of secondary phases, we investigated Er-substituted YIG with only a low Er concentration ($x \leq 0.20$). The actual Er concentrations were determined by ICP-OES measurements and they well matched the nominal Er concentrations of Er:YIG (see Table 1).

To obtain a solid solution of Er-substituted YIG (referred to as Er:YIG, hereafter) with a single phase, Er:YIG was sintered three times at a high temperature above 1300 °C with subsequent inter-grinding, and their crystallographic properties

Table 1. Nominal and Measured Er Concentrations (x) of Er:YIG

nominal x	measured x
$x = 0$	$x = 0.0001$
$x = 0.01$	$x = 0.0088$
$x = 0.05$	$x = 0.0498$
$x = 0.10$	$x = 0.1003$
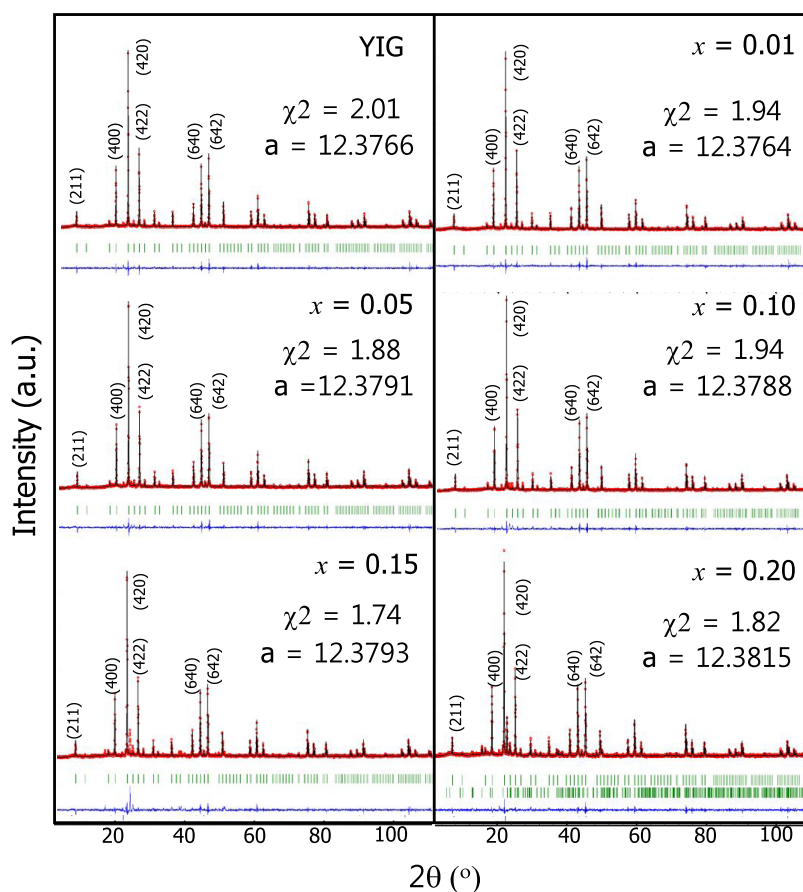
Figure 2. Rietveld refinements of the X-Ray diffraction data of $Y_{3-x}Er_xFe_5O_{12}$ with the Er content (x = 0, 0.01, 0.05, 0.10, 0.15, and 0.20). The experimental and simulated X-ray diffraction are depicted as red dots and black lines, respectively. The difference between the experimental and simulated X-ray diffraction is depicted as a blue line. X-ray diffraction patterns well match the reference peaks of YIG (green bars, space group *Ia-3d*) with a low Er content. In x = 0.20, X-ray diffraction patterns are refined with YIG (upper green bars, space group *Ia-3d*) and $YFeO_3$ (lower green bars, space group *Pnma*).

were examined using X-ray diffraction, as shown in Figure 2. The as-synthesized Er:YIG powder had a cubic structure, and the lattice constants slightly increased with increasing Er content from x = 0 to 0.20. Considering the differences in ionic radii, 0.63 Å (Fe^{3+}), 1.019 Å (Y^{3+}), and 1.144 Å (Er^{3+}), the small increase in the lattice constants of Er:YIG can be explained by Er^{3+} substitution at the Y^{3+} sites in the YIG system.[23]

To study the optical properties of Er:YIG, we conducted FT-IR, UV−VIS, and near IR spectroscopy analyses with $Y_{3-x}Er_xFe_5O_{12}$ powder (x = 0, 0.01, 0.05, and 0.10). The transmittance measurement of $Y_{3-x}Er_xFe_5O_{12}$ in the region of wavenumbers from 400 to 1800 cm^{-1} showed that YIG has strong adsorption at around 450−750 cm^{-1}. Figure 3a shows the FT-IR spectrum of $Y_{3-x}Er_xFe_5O_{12}$ with the Er content (x = 0, 0.01, 0.05, and 0.10) in the region of wavenumbers from 450 to 750 cm^{-1} There were three intense absorption bands, located at around 543, 581, and 646 cm^{-1}, which can be assigned to the asymmetrical stretching vibration of a $Fe_T−O$ tetrahedral in YIG.[24,25] McDevitt et al. reported that the absorption bands in garnets could be shifted linearly with the ionic radius of rare-earth atoms.[26] In the case of Er:YIG, the absorption bands k_1 and k_3 of the Fe−O tetrahedra were red-shifted while k_2 was slightly blue-shifted by increasing Er concentrations (see the trend curves of k_1, k_2, and k_3 in the inset of Figure 3a). Considering the similarity in the ionic

radius of Er^{3+} and Y^{3+}, the red and blue shifts in the adsorption bands might be caused by the local environment changes of the Fe−O tetrahedra, as Er atoms are substituted into Y atomic sites in the YIG system. The absorption bands at around 400 cm^{-1} could be matched to the vibrations of the Fe−O octahedra and Y−O bonds.[24,25]

We also studied the optical properties of Er:YIG in the UV−VIS−NIR range. Figure 3b shows that the Er:YIG has very low reflectance in the VIS range (300−700 nm), and a steep increase in reflectance was observed at around 700 nm. Note that high reflectance exceeding 80% was observed above a wavelength of 1200 nm, which is consistent with the reported high transmittance of YIG in this wavelength range. In Er:YIG with x = 0.05 and 0.10, there are small dips in the wavelengths range of 1450−1550 nm, which correspond to the optical transition between $I_{15/2}$ and $I_{13/2}$ in Er^{3+} ions (see the inset figure in Figure 3b).

We checked the optical bandgaps of Er:YIG using the Tauc plot method, which has been used to estimate the optical bandgap in many semiconducting systems.[27,28] According to the calculated band structures of YIG, YIG with a cubic structure (*Ia-3d*) exhibits a direct bandgap.[29,30] Therefore, we plotted $(\alpha h v)^2$ as a function of the photon energy as shown in Figure 3c. The optical bandgaps deduced from the Tauc plot were around 1.69−1.70 eV over all of the Er concentrations,
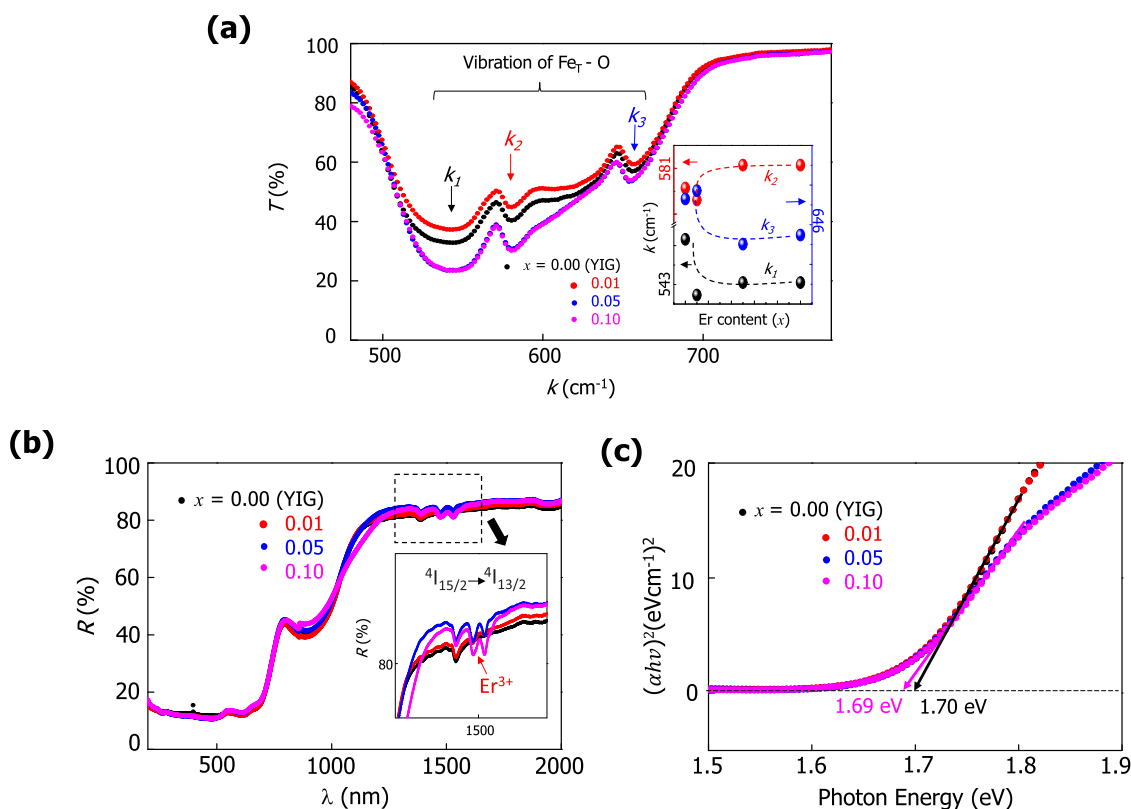
Figure 3. (a) FT-IR spectrum of $Y_{3-x}Er_xFe_5O_{12}$ with the Er content (x = 0, 0.01, 0.05, and 0.10) with three absorption bands, k_1, k_2, and k_3. The inset shows the shifts of k_1, k_2, and k_3 as a function of Er contents (x). (b) UV−VIS−NIR spectrum of $Y_{3-x}Er_xFe_5O_{12}$ with the Er content (x = 0, 0.01, 0.05, and 0.10). The inset shows the optical transition of Er^{3+} in a wavelength range of 1450−1550 nm. (c) Tauc plot of $Y_{3-x}Er_xFe_5O_{12}$ with the Er content (x = 0, 0.01, 0.05, and 0.10) where α is the absorbance and $h\nu$ is an incident photon energy.
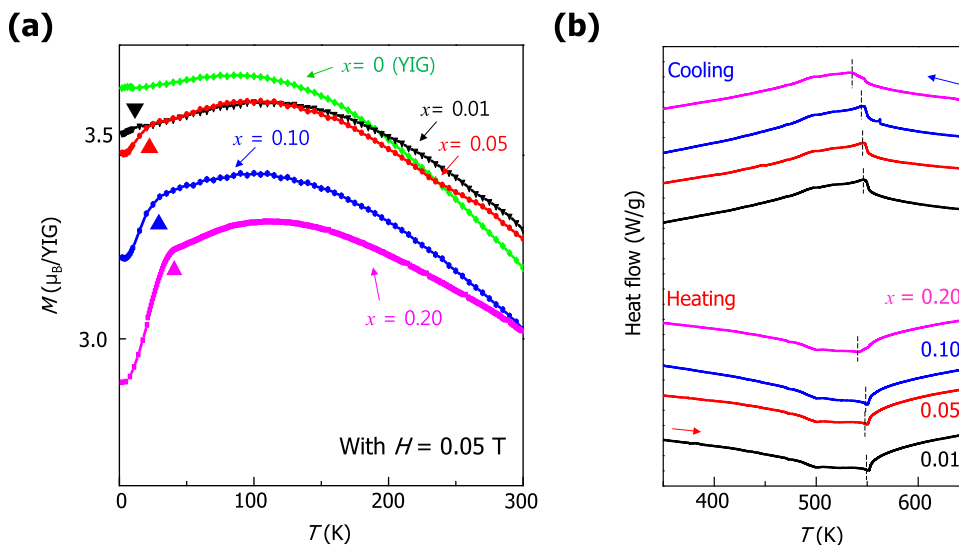
Figure 4. (a) Temperature-dependent magnetic moment of Er:YIG (x = 0, 0.01, 0.05, 0.10, and 0.20) from 2 to 300 K. (b) DSC measurements of $Y_{3-x}Er_xFe_5O_{12}$ with Er content (x = 0, 0.05, 0.10, and 0.20) with a changing temperature between 300 and 700 K upon heating and cooling.

indicating that the optical bandgaps are almost invariant with Er substitution in a slightly Er-substituted YIG system.

The magnetization of YIG originates from the antiferro-magnetically coupled 3d spins of Fe_T and Fe_O. Since Er atoms have a large magnetic moment, exceeding 9.6 μ_B/Er atom, Er substitution at the Y sites can change the magnetic moments of the YIG system. The temperature (T)-dependence of magnet-ization (M) in Er:YIG under a magnetic field of 0.05 T shows

that $Y_{3-x}Er_xFe_5O_{12}$ has ferromagnetic behavior as shown in Figure 5a. The room temperature magnetic moments of $Y_{3-x}Er_xFe_5O_{12}$ with x = 0, 0.01, 0.05, and 0.10 were ~3.0 to 3.3 μ_B per one formula unit. The temperature-dependent magnetic moments of Er:YIG showed that the magnetic moments were saturated or slightly decreased with a decrease in temperature below 100 K. Interestingly, antiferromagnet-like behaviors (dips in magnetization) appeared at low temperatures (<30 K)
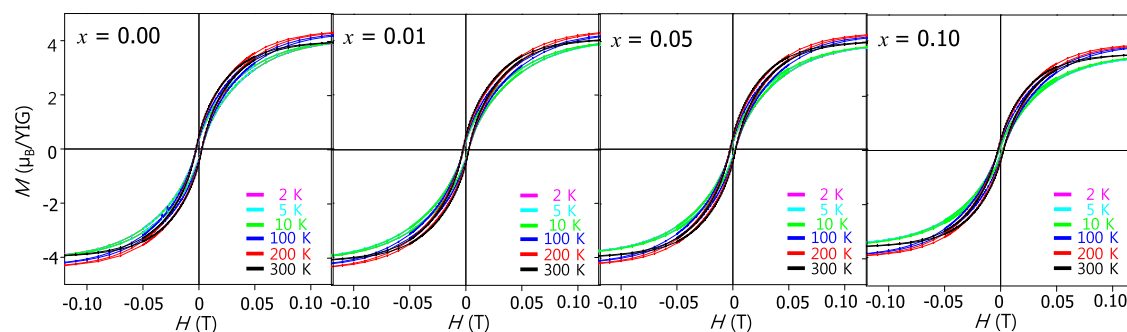
Figure 5. Magnetic field (H) dependency of magnetization in $Y_{3-x}Er_xFe_5O_{12}$ ($x = 0, 0.01, 0.05,$ and 0.10) at various temperatures.
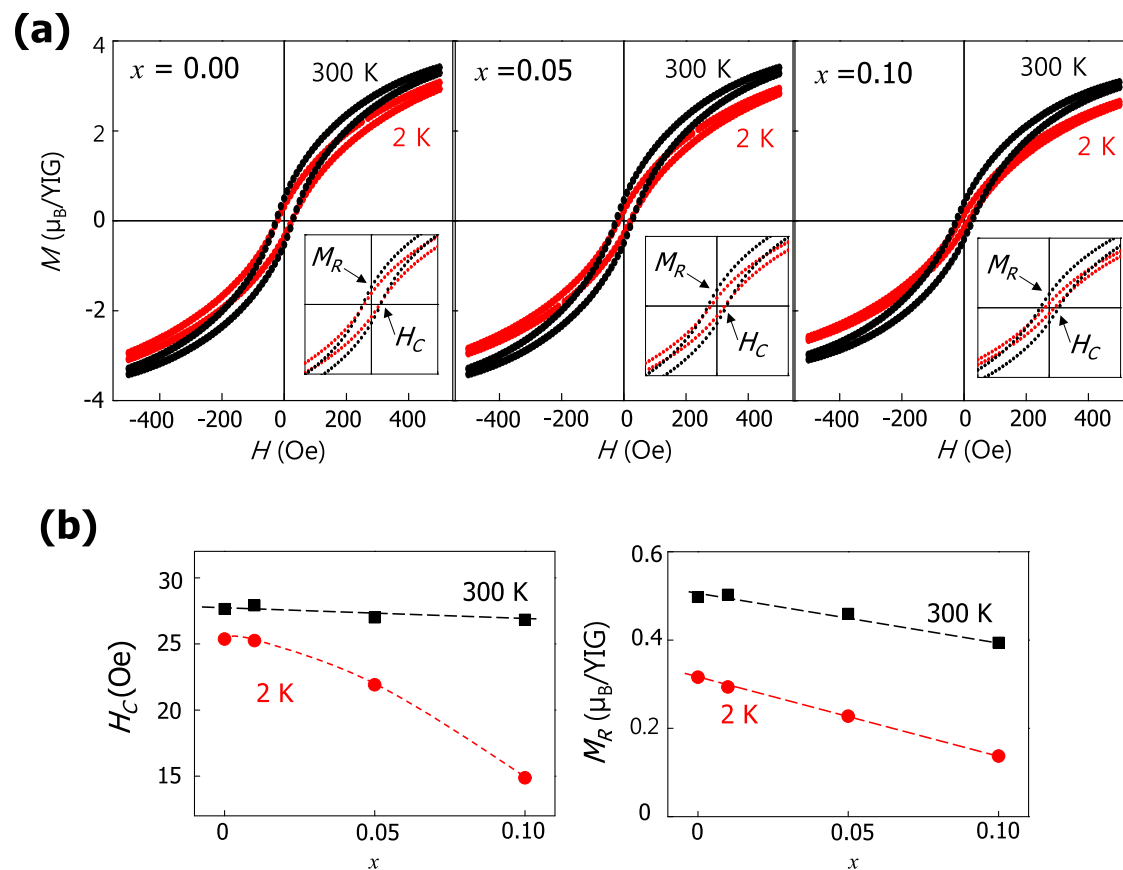

Figure 6. (a) M (H) loops for Er:YIG measured at 2 and 300 K. (b) The coercive force and residual magnetization of Er:YIG as a function of the Er content.

for all of the samples, except for the undoped YIG, which is likely due to the ordering of Er 4f spins in the low-temperature range.[31] The contribution of the Er 4f spins should be dominated by the interactions between Er and the YIG lattice rather than a direct Er−Er interaction because Er 4f orbitals should be much more localized than Fe 3d orbitals and furthermore much farther apart from each other ($\sim$3.8 Å) compared to Er−Fe$_T$ ($\sim$3.10 Å) or Er−Fe$_O$ ($\sim$3.46 Å).[32] The onset temperatures of the dips (referred to as T_{Er} and are denoted by triangles in Figure 5a) increased and the amount of decrease in the magnetic moment below T_{Er} increased with increasing Er concentration, which confirms the conclusion that the dips originated from the weak Er 4f spin ordering. Nevertheless, the presence of Er atoms did not significantly alter the magnetic moments at temperatures above T_{Er} (<30

K), clearly showing that Er 4f spins had a negligible impact on room temperature magnetism.

We estimated the Curie temperatures (T_C) where the ferromagnetic ordering disappeared in Er:YIG using DSC measurements. Upon cooling and heating Er:YIG, an exothermic and endothermic transition occurs at certain temperatures, which are referred to as Curie temperatures (T_C) of Er:YIG.[33] Figure 4 shows the changes of T_C during heating and cooling and are marked with black dashed lines; T_C decreases by roughly 10 K with increasing content of Er from $x = 0$ to 0.20. Considering a reported T_C of YIG at around 560 K,[34] the T_C of the Er:YIG slightly decreases by substituting Er into YIG.

The magnetic field (H) dependence of the magnetization of Er:YIG was measured at various temperatures. Figure 5b shows that the magnetic moments of $Y_{3-x}Er_xFe_5O_{12}$ were saturated
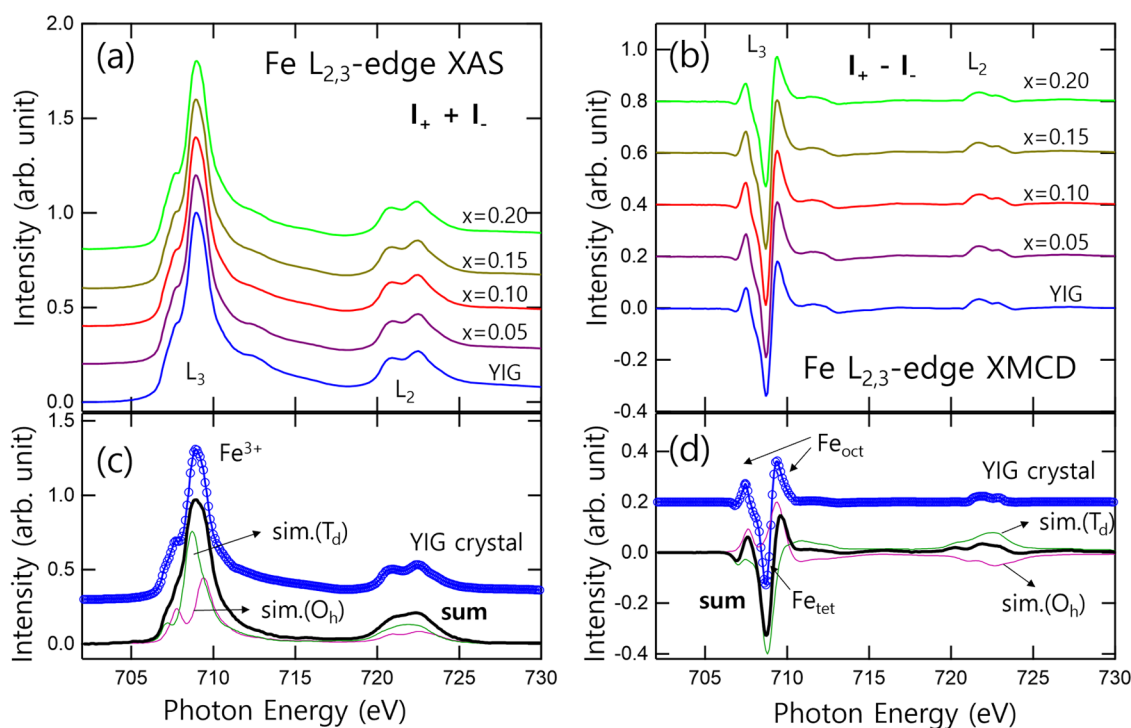
Figure 7. (a) Isotropic term of XAS and (b) XMCD of Er:YIG. The reference spectra of (c) XAS and (d) XMCD from a YIG crystal together with the simulated spectra, adapted with permission from ref 40. Copyrighted by the American Physical Society.

above 0.1 T at a value of around 4.0 μ_B/YIG, which is similar to the theoretically predicted net magnetic moment of YIG (5.0 μ_B/YIG).[35] In a temperature range between 2 and 300 K, the saturated magnetic moments of $Y_{3-x}Er_xFe_5O_{12}$ under a high magnetic field changed slightly with temperature and Er concentrations; however, there were no significant changes in the magnetic properties. The magnetic hysteresis curves of $Y_{3-x}Er_xFe_5O_{12}$ ($x = 0.01, 0.05$, and 0.10) taken at 2 and 300 K were compared as shown in Figure 6a. The magnetic hysteresis curves of $Y_{3-x}Er_xFe_5O_{12}$ were retained up to room temperature with the coercive field (H_C) and residual magnetization (M_R) of $Y_{3-x}Er_xFe_5O_{12}$. The changes in H_C and M_R are explained by impeditive spin ordering at the surface of the Er:YIG powder or the formation of secondary phases.[16,36,37] Figure 6b shows that the H_C and M_R are almost invariant to the Er content at 300 K, while the H_C and M_R at 2 K decrease with the Er content. Therefore, the decrease of H_C and M_R at low temperature are hardly related to particle sizes or impurity phases in Er:YIG. This is likely because antiferromagnetic ordering of Er ions would weaken the ferromagnetic ordering of Fe ions, leading to the decrease of M_S and H_C below T_{Er} (<30 K).

For the XAS and XMCD measurements, the intensities of the XAS signals were collected using circularly polarized X-rays at a magnetic field of $B = 0.7$ T with alternating directions parallel (I_+) and antiparallel (I_-) to the specimens' normal direction. The isotropic spectra ($=I_+ + I_-$) taken at Fe L_3- (photon energy ~709 eV) and L_2-edges (~723 eV) reflect the excited electronic structure of Fe 3d utilizing the strict $2p_{3/2}(2p_{1/2}) \rightarrow 3d$ dipole transition, thereby showing the overall valence and coordination symmetry of the Fe ions irrespective of the magnetism. This implies that the signals from the Fe-containing secondary phase, i.e., $YFeO_3$, were also unavoidably captured. Meanwhile, the difference spectra ($=I_+ - I_-$), called XMCD, capture the signals from the

ferromagnetically ordered Fe ions so as to reveal the electronic structure in ferromagnetic material only. This can help to distinguish the signals from the (Er- substituted) ferromagnetic YIG from that of the antiferromagnetic $YFeO_3$.

Figure 7a shows the isotropic XAS spectra of the Er:YIG powders with targeted Er concentrations of $x = 0, 0.05, 0.1, 0.15$, and 0.2 for $Y_{3-x}Er_xFe_5O_{12}$. Overall, the XAS peak energies can be utilized to measure the average valence of the Fe ions. The energies of the most intense peaks were ~709 eV for all of the samples, which is indicative of a predominant valence of +3 in the Fe ions.[38] Moreover, the XAS lineshapes reflect details of the Fe−O coordination, such as its symmetry and the strength of orbital hybridizations. The spectra are very similar to each other. This suggests identical coordination symmetry of the Fe ions regardless of the Er concentration. The presence of a secondary phase, o-$YFeO_3$ (see Figure 2), might also contribute to the XAS data. However, no significant changes in the lineshapes were observed, even for the Er-rich sample ($x = 0.2$).

The XMCD spectra are displayed in Figure 7b. The intensities of the dips and peaks in the five spectra are almost the same, again indicating negligible evolution of the Fe magnetism with increasing Er concentration. Since o-$YFeO_3$ is almost antiferromagnetic[39] and Er_2O_3 has no Fe ions, the XMCD spectra may be solely due to the local structure and magnetism of the Er:YIG. This indicates that the structure and magnetism in Er:YIG is robust with the inclusion of Er up to $x = 0.2$ despite a small increase in the lattice constant (see Figure 2), and these results are consistent with the robust magnetism of Er:YIG measured using SQUID.

For comparison, the XAS and XMCD spectra of a bulk YIG crystal taken from Chin et al. are appended in Figure 7c,d, respectively.[40] Both spectra can be decomposed into the contributions from two different coordination symmetries of the Fe^{3+} ions in YIG, octahedral (O_h) and tetrahedral (T_d).

The results of the Fe 2p−3d atomic multiplet calculations, which have taken into account the configuration interactions under either the O_h or T_d O ligand field, successfully reproduce the experimental data of YIG.[40]

Thus, each of the peaks and dips in Figure 7b can be due to the signatures of Fe^{3+}−O_h (Fe_O) and Fe^{3+}−T_d (Fe_T): Fe^{3+}−O_h for the two peaks at ∼707 and ∼710 eV, and Fe^{3+}−T_d for the dips at ∼709 eV in the L_3-edge region. The values of Fe_O at the L_3-edge are overall positive (peaks) while those of Fe_T are overall negative (dips). This is because the spins of the Fe_O and Fe_T sites tend to align antiferromagnetically to each other due to super-exchange interactions. The sum of the two XMCDs reproduces the experimental data of Er:YIG, as well as the YIG crystal. Therefore, this confirms that the ratios of the Fe^{3+} ions, $Fe_T/Fe_O = 3/2$, are indeed maintained in Er:YIG.

To elucidate the Y replacement by Er, we conducted Er L_3-edge XAS for Er:YIG with $x = 0.2$ as a representative. Figure 8
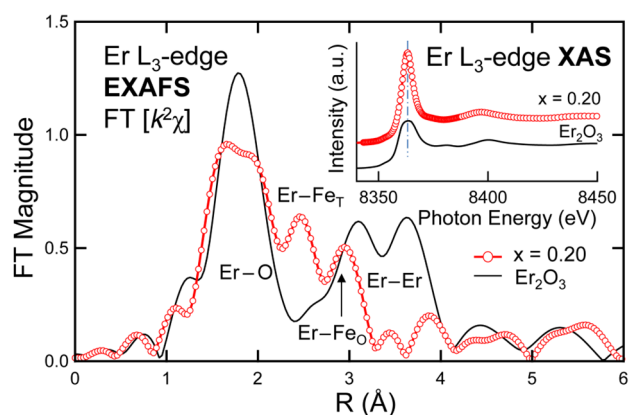
Figure 8. FT magnitudes of k^2-weighted Er L_3-edge EXAFS oscillations (χ) showing the bonding distributions of Er ions in the $x = 0.2$ sample, and the reference Er_2O_3 powder. The XANES results are displayed in the inset.

shows the Fourier-transform (FT) magnitudes of the extended X-ray absorption fine structures (EXAFS) of the $x = 0.2$ sample and a reference Er_2O_3 powder. The FT was processed on k^2-weighted (k: electron momentum) EXAFS in a range of 2−10 Å^{-1} using a Hanning window.[41] The FT EXAFS magnitudes show the bonding distributions of Er ions in both samples. The overall FT spectra are very different from each other, suggesting that the local environment of Er in the $x = 0.2$ sample is fundamentally different from that of Er_2O_3. This confirms that the presence of Er_2O_3 in Er:YIG samples is negligible.

The major peaks were assigned according to the phase uncorrected atomic distance, R, as Er−O, Er−Fe_T, and Er−Fe_O for the $x = 0.2$ sample, and as Er−O and Er−Er for Er_2O_3. The roughly estimated bond lengths ($R + \Delta$) after the scattering phase corrections (Δ) were ∼2.2 to 2.4 Å (Er−O), 2.84 Å (Er−Fe_T), and 3.21 Å (Er−Fe_O), a bit reduced from the bond lengths of 2.37−2.43 Å (Y−O), 3.09 Å (Y−Fe_{tet}), and 3.46 Å (Y−Fe_{oct}) in pristine YIG.[32] The reduction in bond lengths (by 0.1−0.2 Å) appears contradictory to the slightly different size (radius) of Er^{3+} ions (1.144 Å) compared to Y^{3+} ions (1.019 Å). Perhaps, certain local lattice shrinkage is accompanied near Er^{3+} in substituted YIG. We also considered how Er substitution influences three absorption bands in the FT-IR spectra, which correspond to the vibration of the Fe_T−O

tetrahedra. However, the composition dependence of the absorption wavenumbers is rather weak, implying the structural shrinkage occurs only locally.

Meanwhile, the average valence of the Er ions was the same as in Er_2O_3 (that is, 3+). This was confirmed because the first peaks had the same energy (highlighted by the dashed vertical line) in the X-ray absorption near-edge structures (XANES) displayed in the inset. The overall similarity in the Er local structure (EXAFS) as well as in the average valence of Er (XANES) strongly suggests that the Er^{3+} ions indeed occupy the Y sites in the YIG structure. This is consistent with the finding of robustness of the local environment (and thereby the magnetism) of the Fe ions in Figure 7.

The Er^{3+} ions substituting the Y sites can have limited influence on the magnetism in YIG because the magnetism is dominated by the spin interactions of the relatively dispersed Fe 3d orbital states, not the localized Er 4f orbital state. If Er^{3+} occupied Fe_T or Fe_O sites instead, the Fe^{3+} ions leaching from Er:YIG should have constituted a different Fe compound with a distinct local structure (as well as magnetism) from YIG. This is contradictory to the findings of XAS and XMCD in Figure 7, where there are no noticeable changes in the lineshapes observed upon Er doping. Therefore, we concluded that Er doping indeed occurred in YIG (apart from the formation of $YFeO_3$), replacing the Y ions, while the electronic or spin configurations of the Fe ions hardly changed.

Therefore, the decrease in magnetic moments with an increasing Er concentration cannot account for the degradation in Fe 3d ferrimagnetism in YIG. The temperature-dependent magnetization data in Figure 5a show that the magnetic moment decreases gradually as the temperature decreases, even at temperatures above T_{Er} in the low-temperature region (<150 K). Although the Er 4f spins may contribute to the magnetic moments at low temperatures, as in the case of Er_2O_3,[42] the Er 4f electron states should be highly localized in contrast to the delocalized Fe 3d states, so as to be less relevant to the spin transfer, which is the key ingredient in spin devices. This indicates that the loss in spin-transfer functionality induced by the Er substitution would not be substantial.

On the other hand, there is a small but clear evolution in the optical properties (reflectance in the wavelength range of 1450−1550 nm in Figure 3b) due to optical transitions within the Er^{3+} 4f states. Absorption will lead to radiation in the C-band, which is useful for telecommunications. Thus, adding Er offers a promising way of improving optical properties while preserving the magnetic properties in YIG. Further studies are needed to optimize the efficiency of the dopant-related radiation to use YIG-based materials in magneto-optical devices.

IV. CONCLUSIONS

$Y_{3-x}Er_xFe_5O_{12}$ was successfully synthesized with various Er concentrations up to $x = 0.20$ using a solid-state reaction method, and the effects of the Er substitution on the magnetic and optical properties of YIG were scrutinized using various techniques. The Er atoms replacing the Y sites in YIG seemed to modify the optical properties, whereas the magnetic properties were barely modified by the Er substitution except for the contribution of Er 4f spins in the low-temperature regime (T_{Er} < 30 K). The magnetism near room temperature was retained even for the Er-substituted YIG, suggesting that rare-earth ion doping is an effective way of controlling

optoelectronic properties in the mid-infrared range, which is useful for magneto-optical device applications.

■ AUTHOR INFORMATION

Corresponding Authors

　　Deok-Yong Cho − *IPIT and Department of Physics, Jeonbuk National University, Jeonju 54896, Republic of Korea;* ⊙ orcid.org/0000-0001-5789-8286; Email: zax@jbnu.ac.kr

　　Suyeon Cho − *Division of Chemical Engineering and Materials Science, Graduate Program in System Health Science and Engineering, ELTEC College of Engineering, Ewha Womans University, Seoul 03760, Republic of Korea;* ⊙ orcid.org/0000-0003-1931-9663; Email: s.cho@ewha.ac.kr

Authors

　　Yujin Cho − *Division of Chemical Engineering and Materials Science, Graduate Program in System Health Science and Engineering, ELTEC College of Engineering, Ewha Womans University, Seoul 03760, Republic of Korea*

　　Seohui Kang − *Division of Chemical Engineering and Materials Science, Graduate Program in System Health Science and Engineering, ELTEC College of Engineering, Ewha Womans University, Seoul 03760, Republic of Korea*

　　Yeon Woo Nahm − *Division of Chemical Engineering and Materials Science, Graduate Program in System Health Science and Engineering, ELTEC College of Engineering, Ewha Womans University, Seoul 03760, Republic of Korea*

　　Ahmed Yousef Mohamed − *IPIT and Department of Physics, Jeonbuk National University, Jeonju 54896, Republic of Korea*

　　Yejin Kim − *IPIT and Department of Physics, Jeonbuk National University, Jeonju 54896, Republic of Korea*

Complete contact information is available at:
https://pubs.acs.org/10.1021/acsomega.2c01334

Notes

The authors declare no competing financial interest.

■ REFERENCES

(1) Holanda, J.; Major, D. S.; Azevedo, A.; Rezende, M. Detecting the phonon spin in magnon-phonon conversion experiments. *Nat. Phys.* **2018**, *14*, 500−506.

(2) Tabuchi, Y.; Ishino, S.; Ishikawa, T.; Yamazaki, R.; Usami, K.; Nakamura, Y. Hybridizing Ferromagnetic Magnons and Microwave Photons in the Quantum Limit. *Phys. Rev. Lett.* **2014**, *113*, No. 083603.

(3) Bai, L.; Harder, M.; Chen, Y. P.; Fan, X.; Xiao, J. Q.; Hu, C. -M. Spin Pumping in Electrodynamically Coupled Magnon-Photon Systems. *Phys. Rev. Lett.* **2015**, *114*, No. 227201.

(4) Siegel, G.; Prestgard, M. C.; Teng, S.; Tiwari, A. Robust longitudinal spin-Seebeck effect in Bi-YIG thin films. *Sci. Rep.* **2015**, *4*, No. 4429.

(5) Zhong, M.; Hedges, M. P.; Ahlefeldt, R. L.; Bartholomew, J. G.; Beavan, S. E.; Wittig, S. M.; Longdell, J. J.; Sellars, M. J. Optically addressable nuclear spins in a solid with a six-hour coherence time. *Nature* **2015**, *517*, 177−180.

(6) Zhang, X.; Zou, C. L.; Zhu, N.; Marquardt, F.; Jiang, L.; Tang, H. X. Magnon dark modes and gradient memory. *Nat. Commun.* **2015**, *6*, No. 8914.

(7) Huebl, H.; Zollitsch, C. W.; Lotze, J.; Hocke, F.; Greifenstein, M.; Marx, A.; Gross, R.; Goennenwein, S. T. B. High Cooperativity in Coupled Microwave Resonator Ferrimagnetic Insulator Hybrids. *Phys. Rev. Lett.* **2013**, *111*, No. 127003.

(8) Zhang, X.; Zou, C. -L.; jiang, L.; Tang, H. X. Strongly coupled magnons and cavity microwave photons. *Phys. Rev. Lett.* **2014**, *113*, No. 156401.

(9) Goryachev, M.; Farr, W. G.; Creedon, D. L.; Fan, Y.; Kostylev, M.; Tobar, M. E. High-Cooperativity Cavity QED with Magnons at Microwave Frequencies. *Phys. Rev. Appl.* **2014**, *2*, No. 054002.

(10) Tabuchi, Y.; Ishino, S.; Noguchi, A.; Ishikawa, T.; Yamazaki, R.; Usami, K.; Nakamura, Y. Coherent coupling between a ferromagnetic magnon and a superconducting qubit. *Science* **2015**, *349*, 405−408.

(11) Ikesue, A.; Aung, Y. L.; Yasuhara, R.; Iwamoto, Y. Giant Faraday rotation in heavily Ce-doped YIG bulk ceramics. *J. Eur. Ceram. Soc.* **2020**, *40*, 6073−60786074.

(12) Kehlberger, A.; Richter, K.; Onbasli, M. C.; Jakob, G.; Kim, D. H.; Goto, T.; Ross, C. A.; Gotz, G.; Reiss, G.; Kuschel, T.; Klaui, M. Enhanced Magneto-optic Kerr Effect and Magnetic Properties of $CeY_2Fe_5O_{12}$ Epitaxial Thin Films. *Phys. Rev. Appl.* **2015**, *4*, No. 014008.

(13) Saini, T. S.; Sinha, R. K. Mid-infrared supercontinuum generation in soft-glass specialty optical fibers: A review. *Prog. Quantum Electron.* **2021**, *78*, No. 100342.

(14) Thiel, C. W.; Bottger, T.; Cone, R. L. Rare-earth-doped materials for applications in quantum information storage and signal processing. *J. Lumin.* **2011**, *131*, 353−361.

(15) Wei, T.; Tian, Y.; Chen, F.; Cai, M.; Zhang, J.; Jing, X.; Wang, F.; Zhang, Q.; Xu, S. Mid-infrared fluorescence, energy transfer process and rate equation analysis in Er^{3+} doped germanate glass. *Sci. Rep.* **2015**, *4*, No. 6060.

(16) Borade, R. B.; Shirsath, S. E.; Vats, G.; Anil, S.; Patange, S. M.; Kadam, S. B.; Kadam, R. H.; Kadam, A. B. Polycrystalline to preferred-(100) single crystal texture phase transformation of yttrium iron garnet nanoparticles. *Nanoscale Adv.* **2019**, *1*, 403.

(17) Borade, R. B.; Kadam, S. B.; Wagare, D. S.; Kadam, R. H.; Shirsath, S. E.; Nimbore, S. R.; Kadam, A. B. Fabrication of Bi^{3+} substituted yttrium aluminum iron garnet (YAIG) nanoparticles and their structural, magnetic, optical and electrical investigations. *J. Mater. Sci.* **2019**, *30*, 19782−19791.

(18) Princep, A. J.; Ewings, R. A.; Ward, S.; Toth, S.; Dubs, C.; Prabhakaran, D.; Andrew, T. The full magnon spectrum of yttrium iron garnet. *npj Quantum Mater.* **2017**, *2*, 63.

(19) Hapishah, A. N.; Hamidon, M. N.; Syazwan, M. M.; Shafiee, F. N. Effect of grain size on microstructural and magnetic properties of holmium substituted yttrium iron garnets ($Y_{1.5}Ho_{1.5}Fe_5O_{12}$). *Results Phys.* **2019**, *14*, No. 102391.

(20) Cheng, Z.; Yang, H.; Yu, L.; Xu, W. Saturation magnetic properties of $Y_{3-x}Re_xFe_5O_{12}$ (Re: Gd, Dy, Nd, Sm and La) nanoparticles grown by a sol-gel method. *J. Mater. Sci.* **2008**, *19*, 442−447.

(21) Stern, E. A.; Newville, M.; Ravel, B.; Yacoby, Y.; Haskel, D. The UWXAFS analysis package: philosophy and details. *Physica B* **1995**, *208−209*, 117−120.

(22) Mohmed, F.; Dar, F. A.; Rubab, S.; Hussain, M.; Hua, L. Y. Magnetic and thermal properties of ferromagnetic insulator: Yttrium Iron Garnet. *Ceram. Int.* **2019**, *45*, 2418−2424.

(23) Shannon, R. D. Revised Effective Ionic Radii and Systematic Studies of Interatomic Distances in Halides and Chalcogenides. *Acta. Crystallogr.* **1976**, *32*, 751−767.

(24) Ramesh, T.; Shinde, R. S.; Kumar, S.; Murthy, S. R. $Y_{3-x}Gd_xFe_5O_{12}$: controlled synthesis, characterization and investigation of its magnetic properties. *J. Mater. Sci.: Mater. Electron.* **2017**, *28*, 14138−14148.

(25) Fechine, P. B. A.; Silva, E. N.; De Menezes, A. S.; Derov, J.; et al. Synthesis, structure and vibrational properties of $GdIG_X$:YIG_{1-X} ferrimagnetic ceramic composite. *J. Phys. Chem. Solids* **2009**, *70*, 202−209.

(26) McDevitt, N. T. J. Substrate issues for the growth of mercury cadmium telluride. *Opt. Soc. Am.* **1967**, *57*, 827−834.

(27) Dolgonos, A.; Thomas, O. M.; Kenneth, R. Direct optical band gap measurement in polycrystalline semiconductors: A critical look at the Tauc method. *J. Solid State Chem.* **2016**, *240*, 43−48.

(28) Tauc, J. Optical properties and electronic structure of amorphous Ge and Si. *Mater. Res. Bull.* **1968**, *3*, 37−46.

(29) Tao, S.; Hu, C.; Dai, H.; Yang, W.; Liu, H.; Wei, X. First principles study of structure, electronic and optical properties of $Y_3Fe_5O_{12}$ in cubic and trigonal phases. *Mater. Sci.* **2015**, *33*, 169−174.

(30) Larsen, P. K.; Metselaar, R. Defects and the electronic properties of $Y_3Fe_5O_{12}$. *J. Solid State Chem.* **1975**, *12*, 253−258.

(31) Narang, V.; Korakakis, D.; Seehra, M. S. Electronic state of Er in sputtered AIN:Er films determined by magnetic measurements. *J. Appl. Phys.* **2014**, *116*, No. 213911.

(32) Xie, L. S.; Jin, G. X.; He, L.; Gerrit, E. W.; Barker, J.; Xia, K. First-Principles Study of Exchange Interactions of Yttrium Iron Garnet. *Phys. Rev. B* **2017**, *95*, No. 014423.

(33) Ramesh, T.; Shinde, R. S.; Senthil Kumar, S.; Murthy, S. R. $Y_{3-x}Gd_xFe_5O_{12}$: controlled synthesis, characterization and investigation of its magnetic properties. *J. Mater. Sci.* **2017**, *28*, 14138−14148.

(34) Baños-López, E.; Sanchez-De Jesus, F.; Cortes-Escobedo, C. A.; Barba-Pingarron, A.; Bolarín-Miró, A. Enhancement in Curie Temperature of Yttrium Iron Garnet by Doping with Neodymium. *Materials* **2018**, *11*, 1652.

(35) Shaiboub, R.; Ibrahim, N. B.; Abdullah, M.; Abdulhade, F. The Physical Properties of Erbium-Doped Yttrium Iron Garnet Films Prepared by Sol-Gel Method. *J. Nanomater.* **2012**, *2012*, No. 524903.

(36) Musa, M. A.; Azis, R. S.; Osman, N. H.; Hassan, J.; Zangina, T. Structural and magnetic properties of yttrium iron garnet (YIG) and yttrium aluminum iron garnet (YAIG) nanoferrite via sol-gel synthesis. *Results Phys.* **2017**, *7*, 1135−1142.

(37) Jang, M-S.; Ok, H-J.; Oh, I.; Kang, G-H.; Yoo, J-W.; Lee, K-S. Formation of $Y_3Fe_5O_{12}$ matrix including ε-phase Fe_2O_3 with the giant coercive field *via* optimized sol-gel method. *J. Magn. Magn. Mater.* **2022**, *552*, No. 169218.

(38) Zhang, D.; Luo, X. Q.; Wang, Y. P.; Li, T. F.; You, J. Q. Observation of the exceptional point in cavity magnon-polaritons. *Nat. Commun.* **2017**, *8*, No. 1368.

(39) Vasili, H. B.; Casals, B.; Cichelero, R.; Macia, F.; Geshev, J.; Gargiani, P.; Valvidares, M.; Herrero-Martin, J.; Pellegrin, E.; Fontcuberta, J.; Herranz, G. Direct observation of multivalent states and $4f \rightarrow 3d$ charge transfer in Ce-doped yttrium iron garnet thin films. *Phys. Rev. B* **2017**, *96*, No. 014433.

(40) Chin, Y. Y.; Lin, H. −J.; Liao, Y. −F.; Wang, W. C.; Wang, P.; Wu, D.; Singh, A.; Huang, H. −Y.; Chu, Y. −Y.; Huang, D. J.; et al. Local spin moments, valency, and long-range magnetic order in monocrystalline and ultrathin films of $Y_3Fe_5O_{12}$ garnet. *Phys. Rev. B* **2019**, *99*, No. 184407.

(41) Gwon, T.; Mohamed, A. Y.; Yoo, C.; Park, E.-S.; Kim, S.; Yoo, S.; Lee, H.-K.; Cho, D.-Y.; Hwang, C. S. Structural Analyses of Phase Stability in Amorphous and Partially Crystallized Ge-Rich GeTe Films Prepared by Atomic Layer Deposition. *ACS Appl. Mater. Interfaces* **2017**, *9*, 41387−41396.

(42) Han, W.; Maekawa, S.; Xie, X. C. Spin current as a probe of quantum materials. *Nat. Mater.* **2020**, *19*, 139−152.